Dynamical Multiferroicity and Magnetic Topological Structures Induced by the Orbital Angular Momentum of Light in a Nonmagnetic Material

Lingyuan Gao, Sergei Prokhorenko, Yousra Nahas, and Laurent Bellaiche*
Physics Department and Institute for Nanoscience and Engineering, University of Arkansas, Fayetteville, Arkansas 72701, USA

(Received 14 March 2023; accepted 19 September 2023; published 9 November 2023)

Recent studies have revealed that chiral phonons resonantly excited by ultrafast laser pulses carry magnetic moments and can enhance the magnetization of materials. In this work, using first-principles-based simulations, we present a real-space scenario where circular motions of electric dipoles in ultrathin two-dimensional ferroelectric and nonmagnetic films are driven by orbital angular momentum of light via strong coupling between electric dipoles and optical field. Rotations of these dipoles follow the evolving pattern of the optical field and create strong on-site orbital magnetic moments of ions. By characterizing topology of orbital magnetic moments in each 2D layer, we identify the vortex type of topological texture—magnetic merons with a one-half topological charge and robust stability. Our study thus provides alternative approaches for generating magnetic fields and topological textures from light-matter interaction and dynamical multiferroicity in nonmagnetic materials.

DOI: 10.1103/PhysRevLett.131.196801

Spin, as an intrinsic angular momentum of electron, possesses a magnetic dipole moment and has no counterpart in classical mechanics [1]. Spin can be in one of two states, corresponding to either an "up" or "down" magnetic field, leaving it as the main source of ferromagnetism. As a contrast, orbital angular momentum of electrons, resembling orbital motion of classical charges, contributes to another part of the magnetic dipole moment. The definition of orbital angular momentum has gone beyond the motion of electrons and been extended to other charged systems, such as rotating molecules [2,3].

Recently, many efforts have been made in studying effective magnetization caused by ionic motions in solids: as a duality to electric polarization induced by spatially varying spin textures [4,5], emergent magnetization results from the temporally varying electric polarization $\boldsymbol{M} \propto \boldsymbol{P} \times \partial_t \boldsymbol{P}$ [6–11]. Such dynamical polarization can be produced by driving collective motions of ions, usually termed as "phonons" in solid-state language. The cross product between $\boldsymbol{P}$ and its time-derivative $\partial_t \boldsymbol{P}$ further requires ions to move on a closed orbit and to carry an orbital angular momentum, and that corresponds to chiral or circularly polarized phonons [12–17]. In reciprocal space, chiral phonons are located at high symmetry points either at the center or the boundary of the Brillouin zone [14,17–20]. At the zone center, chiral phonons exist as a superposition of two orthogonal, degenerate phonon modes; while at the zone edges, recent experiments show that nondegenerate chiral phonons are observed in crystals with hexagonal symmetries [14,19].

Moreover, numerous studies show that light can control the magnetization in crystals by driving optical phonon modes and tuning structural distortions [21–28]. At the zone center, infared (IR)- and Raman-active modes, related to electric polarization and polarizability, respectively, can be excited with an ultrafast terahertz (THz) laser pulse. Specifically, a degenerate chiral phonon can be excited by a circularly polarized light [17,29]. At the zone edge, chiral phonon is not permitted to be excited by light, due to the large mismatch between momenta of phonons and photons. Recent studies predicted and demonstrated that cerium trihalides are capable of generating strong effective magnetic fields by exciting chiral phonons with circularly polarized THz pulses [28,30].

In this work, we propose an alternative approach to induce effective magnetic field established on the mechanism of dynamical multiferroicity. Instead of focusing on coherently excited chiral phonons, we drive circular motions of ions with a particular type of light—optical vortex (OV) beam. Such light carries an orbital angular momentum (OAM) [31–33], and can exert OAM to manipulate the motion of microparticles as an optical tweezer [34–36]. Here we demonstrate that OAM can be transferred from the light to the motion of ions via the coupling between electric dipoles and optical field. As a prototype example, we use first-principles-based simulations and demonstrate that in ultrathin ferroelectric $Pb(Zr,Ti)O_3$ films, microscopic electric dipoles indeed rotate with the time-varying OAM field. As a result, orbital magnetic moments of ions are effectively generated resulting in a non-negligible magnetic field even in nonmagnetic materials. This differs from previously proposed mechanisms in that in a confined system, the real-space circular motion of ions at each site directly follows the pattern of the

optical field, rather than move along the phonon eigenvectors. Here the resulting displacements have much larger amplitudes than the displacements caused by phonons, which result in much larger dynamical magnetic moments. This largely broadens the range of candidate materials restricted by crystal symmetry as well as light frequencies, so that the effect of dynamical multiferroicity can be tuned more freely. More intriguingly, at specific times, microscopic magnetic moments on a single layer of this quasi-2D system are arranged in a vortex-type configuration, proving topological magnetic structures—magnetic merons—can also be produced out of orbital magnetic moments of ions and dynamical multiferroicity.

We perform first-principles-based effective Hamiltonian (H_{eff}) molecular dynamics (MD) calculations to conduct this time-dependent study [37,38]. H_{eff} represents low-order energy expansions in structural distortions relative to a highly symmetric configuration, and it depends on the following specific variables: local soft mode $\boldsymbol{u}_i$ where i refers to the atomic site index, homogeneous strain tensor η, and inhomogeneous strain variable $\boldsymbol{v}_i$. All parameters of H_{eff} are fitted from first principles from calculations, especially for the acoustic phonon and soft optical phonon branches that are most responsible for structural distortions during phase transitions. The effect of external electric field $\boldsymbol{E}(\vec{r})$ is incorporated by including a $-\sum \boldsymbol{p}_i \cdot \boldsymbol{E}_i$ term in the H_{eff} energy [39,40], where $\boldsymbol{p}_i$ is the local electric dipole moment that is directly proportional to the local soft mode $\boldsymbol{u}_i$ by a factor of Born effective charge Z^*. The effective Hamiltonian has been well developed for $Pb(Zr,Ti)O_3$ systems and has made a series of successful predictions about topological structures and phase transitions, which were then confirmed by experiments [41–49]. Here, we model $Pb(Zr_{0.4}Ti_{0.6})O_3$ (PZT) ferroelectric ultrathin films grown along the [001] direction with an $80 \times 80 \times 8$ supercell, which is periodic along the two in-plane directions [100] and [010] but finite along the out-of-plane [001] direction with one substrate layer (layer 1) on the bottom and two vacuum layers on the top (layers 7, 8). Note that the local heating effect from field with large amplitudes could also reshape the structural textures, but at a much slower speed [50,51]. Furthermore, with a current set of parameters, we estimate the increasing temperature brought by the OV beam and find that the heating effect is negligible (see Supplemental Material [52], which includes Refs. [53–81]).

The OV beam is introduced as the lowest order ($l = 0$) of the "Laguerre-Gaussian" mode [31,82], and the electric field is written as

$$\vec{E}(\vec{r},t) = E_0 \left(\frac{\sqrt{2}\rho}{w}\right)^{|m|} e^{-\frac{\rho^2}{w^2}} \big(\cos(m\phi - \omega t)\vec{e}_x - \sigma \sin(m\phi - \omega t)\vec{e}_y\big). \quad (1)$$

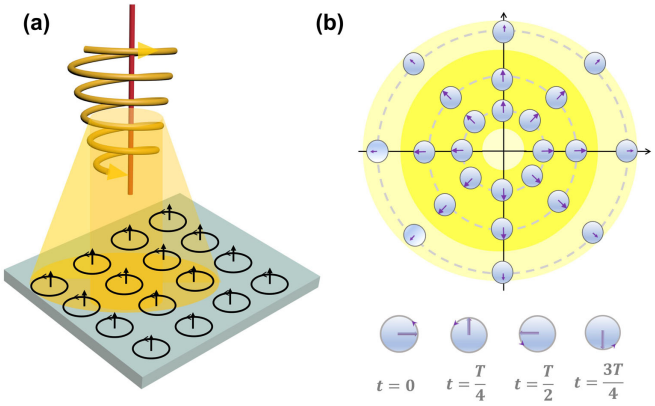

FIG. 1. Illustration of ferroelectric PZT films illuminated by OV beam. (a) OV beam with a helical wavefront is normally incident on PZT films. Current loops form at each site due to the rotation of electric dipoles, which induce emergent magnetic moments (black arrows pointing up). (b) The distribution of in-plane components of local soft mode vectors $u_{x,y}$ (denoted by arrows) on each site (gray sphere) at $t = nT$ after the system establishes cyclic motion. We draw polar coordinates with its origin coinciding with the center of the (001) plane to denote the thin film plane and three circles in radius of $0.5w$, w, and $2w$, colors of which indicate the variation of the E field intensity along the radial direction. The bottom part depicts the change of the dipole's orientation with time at a selected site.

In the equation above, $\vec{e}_x$ and $\vec{e}_y$ are two light polarization vectors pointing along the [100] and [010] in-plane directions, respectively. E_0 and ω denote the magnitude and frequency of the electric field, respectively; considering the response time of electric dipoles is typically at the picosecond level, we set $\omega = 1$ THz, and we chose $E_0 = 18 \times 10^9$ V/m. ρ and ϕ are radial distance and azimuth angle in cylindrical coordinates (ρ, ϕ, z), and w is the beam width at the wavefront $z = 0$; considering the dimension of the system, we set $w = 7$ unit cells (u.c.). The integer m and σ characterize the phase twist of the field and the handedness of the polarization, corresponding to orbital and spin angular momentum, respectively. Their product $-m \cdot \sigma$ gives the winding number of the field [83]. In this work, we choose $\sigma = 1$ and $m = -1$. We describe other computational details and explain the feasibility of designing such optical field in experiment in the Supplemental Material [52].

Figure 1(a) illustrates the interaction between the OV beam and the PZT films. The light is normally incident onto the (001) plane, and we let the beam pass through the center of the plane. In contrast with linearly and circularly polarized lights for which the polarized electric field has a line-shape profile, the electric field of the OV beam at the wavefront has a circular shape; also, the field vector $\vec{E}(\vec{r},t)$ changes its orientation with both azimuth angle ϕ and time t. According to Eq. (1), the factor $\rho e^{-(\rho^2/w^2)}$ dictates that, along the radial

direction, the field intensity $E(\rho)$ first increases and then decreases.

The initial configuration in PZT film without OV beam is a homogeneously polarized state (i.e., a monodomain) due to good screening and compressive misfit strain, where all electric dipoles are aligned and point down with out-of-plane p_z components. After turning on the light and when the cyclic dynamics is well established, the local soft modes develop an in-plane component $u_{x,y}(\vec{r},t)$ parallel to the local $E_{x,y}(\vec{r},t)$. Such local in-plane polarization is due to the $-\boldsymbol{P}\cdot\boldsymbol{E}$ coupling and appears in addition to the original p_z component reminiscent of the original poled domain. As an example, Fig. 1(b) illustrates that at the moment $t = nT$ (where n is an integer and T is the period of the OV beam), $u_{x,y}(\vec{r})$ exhibits a divergent distribution pattern with all $u_{x,y}(\vec{r})$ directed radially outward, similar to the synchronous distribution of $E_{x,y}(\vec{r})$ on the film's plane. As demonstrated in the bottom part of Fig. 1(b), at each site, $u_{x,y}(\vec{r},t)$ will rotate in an anticlockwise way following the evolution of $E_{x,y}(\vec{r},t)$. In the classical point-charge model [3,84], individual rotating electric dipole induces the current loop formed at each site. This rotation produces microscopic magnetic moments and these latter overall add up to a macroscopic magnetic field [see illustration in Fig. 1(a)].

Figure 2 shows plots of $u_{x,y}(t)$ *versus* time at characteristic sites. Figures 2(a) and 2(b) show $u_{x,y}(t)$ of sites at $\phi = 0°$ and 180° [namely, the x axis of the coordinates displayed in Fig. 1(b)]: both $u_{x,y}(t)$ at sites 7 u.c.($1w$) and 4 u.c.($0.5w$) from the center display sine or cosine pattern with close amplitudes, resulting from similar electric field magnitudes at these two distances. The periodicity is 1 ps consistent with the frequency of 1 THz OV beam, and the initial displacement of $u_{x,y}$ at $t = 2$ ps is settled by the azimuth angle ϕ. Note the maxima or minima of $u_{x,y}(t)$ have a 0.05 ps delay relative to the maxima or minima of local $E_{x,y}(t)$ due to the response time of electric dipole to local field. At sites 14 u.c.($2w$) from the center, periodic profiles of $u_{x,y}(t)$ deviate from the sine or cosine pattern with largely reduced amplitudes, indicating that at small local field, $u_{x,y}(t)$ do not closely follow $E_{x,y}(t)$. According to symmetry, by interchanging $u_x \leftrightarrow u_y$, $u_{x,y}(t)$ of sites at $\phi = 90°$ and 270° [the y axis of the coordinates displayed in Fig. 1(b)] in Figs. 2(c) and 2(d) are just replica of Figs. 2(a) and 2(b), only up to a shift of 0.5 ps to compensate the phase difference. These mode displacements indicate that the winding pattern and orbital angular momentum are indeed transferred from light to local soft modes owing to their mutual couplings.

Now we start to analyze the effective magnetic field from the rotation of local soft modes or, equivalently, electric dipoles. Enlightened by previous derivations about the magnetic moment induced by steady current, moving

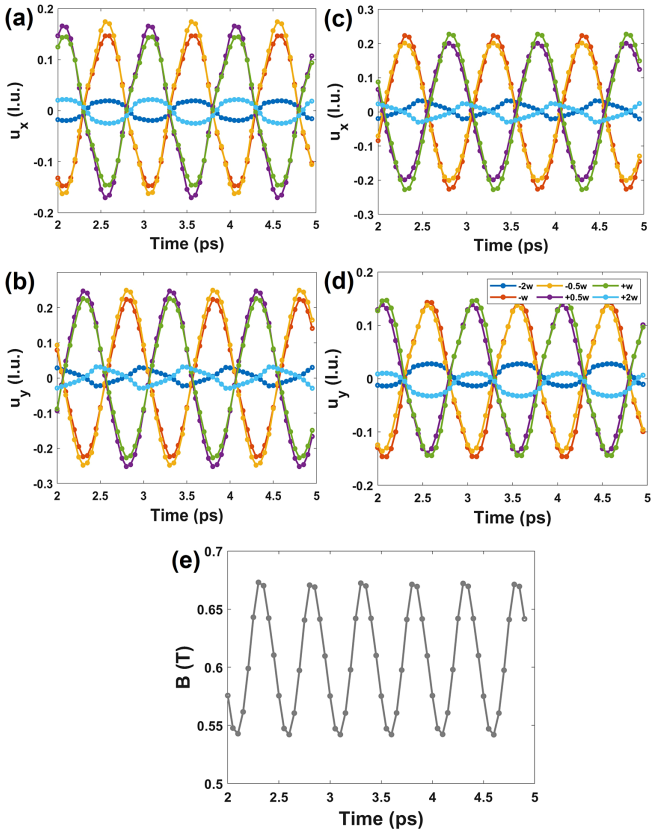

FIG. 2. (a)–(d) The variation of $u_{x,y}(\vec{r},t)$ at different sites with time. In accordance with the coordinates displayed in Fig. 1(b), $u_{x,y}$ associated with 6 sites on the x axis of the coordinates are shown in (a),(b), while $u_{x,y}$ associated with 6 sites on the y axis are shown in (c),(d). In the legend, the "+" and "−" signs denote whether sites are located on the positive or negative side of the axes, respectively. "xw" ($x = 0.5\times, 1\times, 2\times$, and w is the beam radius of 7 u.c.) denotes the distance from the site to the center. $u_{x,y}$ is in the unit of lattice constant (3.99 Å as 1 u.c.). (e) The effective magnetic field generated in the PZT system illuminated by the OV beam.

charges and circular phonons [3,84], the on-site orbital magnetic moment is given by

$$\boldsymbol{m}_i = \frac{Z^* e}{2}\boldsymbol{u}_i \times \frac{d\boldsymbol{u}_i}{dt}, \tag{2}$$

where e is the elementary charge of the electron (see Supplemental Material [52] for detailed derivation). This equation can be directly used in the effective Hamiltonian approach to compute microscopic $\boldsymbol{m}_i$.

Histograms in the Supplemental Material [52] show that at all times, on-site m_i are distributed in the range of $5\times10^{-8} \sim 3\times10^{-3}\mu_B$. By approximating $\boldsymbol{B}_i$ by $\mu_0\boldsymbol{m}_i/V$, where V is the volume of the unit cell and μ_0 is the vacuum permeability, and summing over all sites in the system, we compute the z component of the effective magnetic field $B_z(t)$ and plot it *versus* time in Fig. 2(e). As $B_z(t) \sim u(t)^2$,

the frequency is doubled and it has a period about 0.5 ps. The magnitude of the total magnetic field varies between $0.55T$ and $0.65T$, much more dramatic compared to the dynamical magnetic field from a moving charged domain wall where the magnetic moment and magnetic field per cell is $2.5 \times 10^{-5}\mu_B$ and 4.5 μT, respectively [80]. We note that a very recent work studied dynamical multiferroicity in $SrTiO_3$ illuminated by circularly-polarized THz field and reported a simulation value of m_i around $0.01\mu_B$ [28], larger than the maximal m_i in our calculation. Though with different origins, both works demonstrate that generating strong magnetic field with dynamical multiferroicity via THz light is feasible.

In contrast to $B_z(t)$, the net in-plane magnetic field $B_{x,y}(t)$ vanishes, owing to a symmetric distribution of $\boldsymbol{m}_i(t)$ within each plane. As an example, Figs. 3(a) and 3(b) display full in-plane views of the $m_{x,y}$ distribution at time 3.3 ps on layer 2 and layer 6, respectively. Both layers present vortex ring structures with left-hand circulation, and $m_{x,y}$ spans a full 360° when it goes along ϕ for a full circle. Nevertheless, the vortex on layer 6 is divergent with the central $m_{x,y}$ pointing outwards, while the vortex on layer 2 is convergent with central $m_{x,y}$ pointing inwards. As revealed in our previous study [85], the out-of-plane component of electric dipoles p_z vary with time as an electrostatic response to the time-varying $p_{x,y}$: at time 3.3 ps, all layers have negative p_z and share a similar anticlockwise pattern for $p_{x,y}$, while layer 2 has negative dp_z/dt but layer 6 has positive dp_z/dt in the central region. Mutual products between dp_z/dt and $p_{x,y}$, and between $dp_{x,y}/dt$ and dp_z induce magnetic merons with their configuration differing between different layers. Figure 3(c) gives a section view when the system is cut through $y = 40$, and it presents m_x and m_z at sites on the x axis for all five layers. With an increasing ρ, m_x decreases while the out-of-plane m_z develops to be the major component; for ρ larger than 7 u.c.(w), m_z starts to decrease, and m_i becomes much smaller at sites 14 u.c.($2w$) from the center. The positive m_z at each site and the chirality of vortices are settled by the left-hand polarization of the light and the counterclockwise rotating $p_{x,y}$.

We characterize the topology of magnetic vortex ring on each layer, by computing the Pontryagin charge density ρ_{sk} and then integrating it over the full plane:

$$N_{sk} = \int \rho(\vec{r}) d^2\vec{r} = \int \frac{1}{4\pi}\vec{n}(\vec{r}) \cdot \left(\frac{\partial \vec{n}(\vec{r})}{\partial x} \times \frac{\partial \vec{n}(\vec{r})}{\partial y}\right) d^2\vec{r}, \quad (3)$$

where $\vec{n}(\vec{r})$ is the normalized magnetic moment vector at site $\vec{r}$. Note at some sites, especially far from the center, m_i are several orders of magnitudes smaller compared to m_i within beam radius; therefore, we round up each component of m_i at an accuracy of $10^{-5}\mu_\beta$, so that m_i smaller than the threshold value are excluded in contributing to field topology.

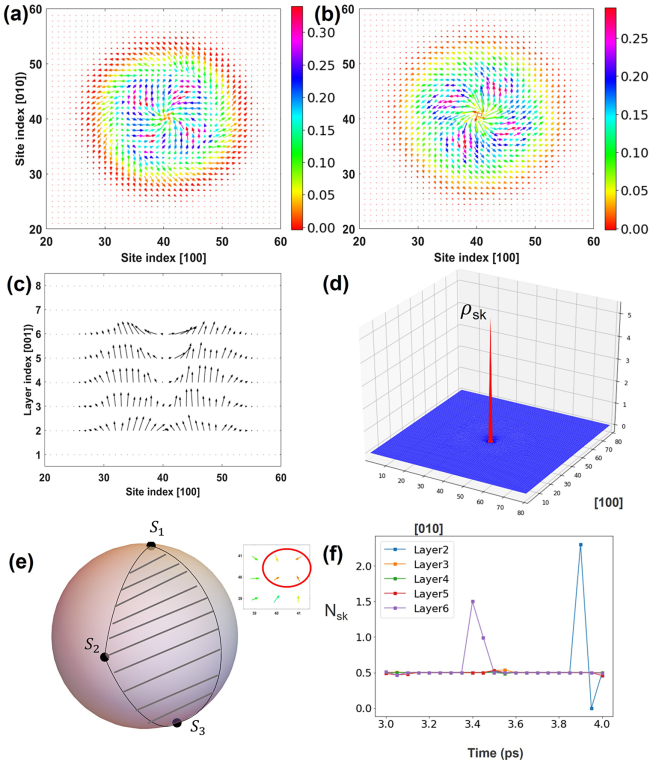

FIG. 3. (a) In-plane view of the magnetic moment configuration on layer 2 at $t = 3.3$ ps, with arbitrary units. The horizontal and vertical axes denote the site number along the x and y directions, respectively. In-plane arrows denote $m_{x,y}$ and the color denotes m_z. (b) Similar to (a), but on layer 6 at $t = 3.3$ ps. (c) Section view of the magnetic moment configuration in the $y = 40$ plane at $t = 3.3$ ps. The horizontal and vertical axes denote the site number along the x direction and the layer number along the z direction, respectively. The arrows denote m_x and m_z components. (d) Topological charge density map ρ_{sk} on layer 2 at $t = 3.3$ ps. (e) Spherical triangles set by three orbital magnetic moments $\boldsymbol{m}_i$ on sites (40, 40), (41, 40), and (41, 41), respectively. Vertices S_1, S_2, and S_3 are projections of three $\boldsymbol{m}_i$ on the sphere. An enlarged in-plane view of these moments are presented in the inset. (f) The variation of topological number N with time for each layer during 3–4 ps.

The computed topological charge N_{sk} is 0.5 for all five layers at 3.3 ps, consistent with direct observation in Figs. 3(a)–3(c) that $\boldsymbol{m}_i$ on each layer cover the whole hemisphere in three-dimensional order parameter space. This demonstrates that "meronlike" objects, as one half of skyrmions, are created [86–89]. Distinguished from spin magnetic moment and asymmetric magnetic exchange interactions, where usually merons and antimerons appear in pairs [90–93], here antimerons in the shape of antivortex and with an opposite charge $N_{sk} = -0.5$ are not observed; also, the merons do not emerge from a uniform background field.

The distribution of ρ_{sk} on layer 2 is shown in Fig. 3(d), and we identify a sharp charge density peak localized at the center. In a discrete lattice model, ρ_{sk} is computed as the area of spherical triangle whose vertices are projected field vectors at three neighboring sites [81]. The large ρ_{sk} at the center corresponds to a swirling configuration where $\boldsymbol{m}_{x,y}$ at site (40, 40) are almost antiparallel to $\boldsymbol{m}_{x,y}$ at site (41, 41) along the diagonal [110] direction, and are almost orthogonal to $\boldsymbol{m}_{x,y}$ at site (41, 40) [and $\boldsymbol{m}_{x,y}$ at (40, 41)], as shown in the inset of Fig. 3(e). When unit vectors of $\boldsymbol{m}_1$, $\boldsymbol{m}_2$, and $\boldsymbol{m}_3$ (or $\boldsymbol{m}_1$, $\boldsymbol{m}_3$, and $\boldsymbol{m}_4$) are projected onto the surface of the 3D sphere [Fig. 3(e)], great arcs passing these vertices enclose spherical triangles with large area and result in large ρ_{sk}, as shown in Fig. 3(e).

We also compute topological charges N_{sk} at other times and plot them in Fig. 3(f). Stabilities of magnetic merons and $N_{sk} = 0.5$ for all five layers are well maintained between 3.15–3.35 and 3.6–3.85 ps, while between 3.0–3.1 and 3.5–3.55 ps, N_{sk} for some layers deviate from 0.5 slightly. Interestingly, N_{sk} of layer 6 at 3.4–3.45 ps and N_{sk} of layer 2 at 3.9–3.95 ps significantly differ from 0.5. As revealed in the Supplemental Material [52], this is associated with more than one sharp ρ_{sk} peak and swirling configuration of $\boldsymbol{m}_i$ residing at different places within the layer. Since $\boldsymbol{m}_i$ originates from variation of electric dipoles $\boldsymbol{p}_i$, this demonstrates that at these moments, local $\boldsymbol{p}_i$ vary differently at interfacial layers compared to other layers. Note that ferroelectric skyrmions only form at layer 2 and layer 6 and the inversion of p_z occurs when N_{sk} of the respective layer is far from 0.5 [85]. We present the detailed variation of $\boldsymbol{p}_i$ resolved on each layer in the Supplemental Material [52].

In conclusion, using first-principles-based atomistic methods, we demonstrate that magnetic fields can be induced in ferroelectric but nonmagnetic PZT ultrathin films under illumination by an optical vortex beam. Orbital angular momentum is transferred from the optical field to local soft modes, and rotations of electric dipoles produce loop current and the resultant orbital magnetic moment of ions. We further identify formation of magnetic merons by characterizing orientations of magnetic moments on different layers. Our study compliments the frequently discussed "excitations of chiral phonon" as an alternative way to put dynamical multiferroicity into practice. In experiment, the dynamical multiferroicity induced in PZT thin films can be quantified by measuring the time-resolved Kerr ellipticity [28,30], while the induced magnetic merons can be visualized by Lorentz transmission electron microscopy [94–97].

We thank Professor Dominik Maximilian Juraschek and Professor Surendra Singh for valuable discussions. We acknowledge the support from the Grant MURI ETHOS W911NF-21-2-0162 from Army Research Office (ARO), the Vannevar Bush Faculty Fellowship (VBFF) Grant No. N00014-20-1-2834 from the Department of Defense and Award No. DMR-1906383 from the National Science Foundation Q-AMASE-i Program (MonArk NSF Quantum Foundry). We also acknowledge the computational support from the Arkansas High Performance Computing Center and HPCMP Pathfinder Award for computational resources.

*Corresponding author: laurent@uark.edu

[1] A. S. Mahajan and A. A. Rangwala, *Electricity and Magnetism* (Tata McGraw-Hill, New Delhi, 2001).
[2] G. Wick, On the magnetic field of a rotating molecule, Phys. Rev. **73**, 51 (1948).
[3] J. D. Jackson, *Classical Electrodynamics* (Wiley, New York, 1999).
[4] M. Mostovoy, Ferroelectricity in spiral magnets, Phys. Rev. Lett. **96**, 067601 (2006).
[5] S.-W. Cheong and M. Mostovoy, Multiferroics: A magnetic twist for ferroelectricity, Nat. Mater. **6**, 13 (2007).
[6] S. Prosandeev, A. Malashevich, I. P. Raevski, and L. Bellaiche, Dynamical magnetoelectric effects associated with ferroelectric domain walls, Phys. Rev. B **91**, 100101(R) (2015).
[7] D. M. Juraschek, M. Fechner, A. V. Balatsky, and N. A. Spaldin, Dynamical multiferroicity, Phys. Rev. Mater. **1**, 014401 (2017).
[8] D. M. Juraschek and N. A. Spaldin, Orbital magnetic moments of phonons, Phys. Rev. Mater. **3**, 064405 (2019).
[9] R. M. Geilhufe, V. Juričić, S. Bonetti, J.-X. Zhu, and A. V. Balatsky, Dynamically induced magnetism in $KTaO_3$, Phys. Rev. Res. **3**, L022011 (2021).
[10] D. M. Juraschek, T. Neuman, and P. Narang, Giant effective magnetic fields from optically driven chiral phonons in 4 f paramagnets, Phys. Rev. Res. **4**, 013129 (2022).
[11] G. Xiong, H. Chen, D. Ma, and L. Zhang, Effective magnetic fields induced by chiral phonons, Phys. Rev. B **106**, 144302 (2022).
[12] L. Zhang and Q. Niu, Angular momentum of phonons and the Einstein–de Haas effect, Phys. Rev. Lett. **112**, 085503 (2014).
[13] L. Zhang and Q. Niu, Chiral phonons at high-symmetry points in monolayer hexagonal lattices, Phys. Rev. Lett. **115**, 115502 (2015).
[14] H. Zhu, J. Yi, M.-Y. Li, J. Xiao, L. Zhang, C.-W. Yang, R. A. Kaindl, L.-J. Li, Y. Wang, and X. Zhang, Observation of chiral phonons, Science **359**, 579 (2018).
[15] L. Du, J. Tang, Y. Zhao, X. Li, R. Yang, X. Hu, X. Bai, X. Wang, K. Watanabe, T. Taniguchi *et al.*, Lattice dynamics, phonon chirality, and spin–phonon coupling in 2d itinerant ferromagnet Fe_3GeTe_2, Adv. Funct. Mater. **29**, 1904734 (2019).
[16] T. Yin, K. A. Ulman, S. Liu, A. Granados del Águila, Y. Huang, L. Zhang, M. Serra, D. Sedmidubsky, Z. Sofer, S. Y. Quek *et al.*, Chiral phonons and giant magneto-optical effect in $CrBr_3$ 2d magnet, Adv. Mater. **33**, 2101618 (2021).

[17] K. Ishito, H. Mao, Y. Kousaka, Y. Togawa, S. Iwasaki, T. Zhang, S. Murakami, J.-i. Kishine, and T. Satoh, Truly chiral phonons in α-HgS, Nat. Phys. **19**, 35 (2023).

[18] Y. Tatsumi, T. Kaneko, and R. Saito, Conservation law of angular momentum in helicity-dependent Raman and Rayleigh scattering, Phys. Rev. B **97**, 195444 (2018).

[19] X. Chen, X. Lu, S. Dubey, Q. Yao, S. Liu, X. Wang, Q. Xiong, L. Zhang, and A. Srivastava, Entanglement of single-photons and chiral phonons in atomically thin WSe2, Nat. Phys. **15**, 221 (2019).

[20] C. Chen, X. Chen, B. Deng, K. Watanabe, T. Taniguchi, S. Huang, and F. Xia, Probing interlayer interaction via chiral phonons in layered honeycomb materials, Phys. Rev. B **103**, 035405 (2021).

[21] T. F. Nova, A. Cartella, A. Cantaluppi, M. Först, D. Bossini, R. V. Mikhaylovskiy, A. V. Kimel, R. Merlin, and A. Cavalleri, An effective magnetic field from optically driven phonons, Nat. Phys. **13**, 132 (2017).

[22] S. F. Maehrlein, I. Radu, P. Maldonado, A. Paarmann, M. Gensch, A. M. Kalashnikova, R. V. Pisarev, M. Wolf, P. M. Oppeneer, J. Barker *et al.*, Dissecting spin-phonon equilibration in ferrimagnetic insulators by ultrafast lattice excitation, Sci. Adv. **4**, eaar5164 (2018).

[23] P. G. Radaelli, Breaking symmetry with light: Ultrafast ferroelectricity and magnetism from three-phonon coupling, Phys. Rev. B **97**, 085145 (2018).

[24] M. Fechner, A. Sukhov, L. Chotorlishvili, C. Kenel, J. Berakdar, and N. A. Spaldin, Magnetophononics: Ultrafast spin control through the lattice, Phys. Rev. Mater. **2**, 064401 (2018).

[25] G. Khalsa and N. A. Benedek, Ultrafast optically induced ferromagnetic/anti-ferromagnetic phase transition in $GdTiO_3$ from first principles, npj Quantum Mater. **3**, 15 (2018).

[26] D. Afanasiev, J. Hortensius, B. Ivanov, A. Sasani, E. Bousquet, Y. Blanter, R. Mikhaylovskiy, A. Kimel, and A. Caviglia, Ultrafast control of magnetic interactions via light-driven phonons, Nat. Mater. **20**, 607 (2021).

[27] A. Stupakiewicz, C. Davies, K. Szerenos, D. Afanasiev, K. Rabinovich, A. Boris, A. Caviglia, A. Kimel, and A. Kirilyuk, Ultrafast phononic switching of magnetization, Nat. Phys. **17**, 489 (2021).

[28] M. Basini, M. Pancaldi, B. Wehinger, M. Udina, T. Tadano, M. Hoffmann, A. Balatsky, and S. Bonetti, Terahertz electric-field driven dynamical multiferroicity in $SrTiO_3$, arXiv:2210.01690.

[29] K. Ishito, H. Mao, K. Kobayashi, Y. Kousaka, Y. Togawa, H. Kusunose, J.-i. Kishine, and T. Satoh, Chiral phonons: Circularly polarized raman spectroscopy and *ab initio* calculations in a chiral crystal tellurium, Chirality **35**, 338 (2023).

[30] J. Luo, T. Lin, J. Zhang, X. Chen, E. R. Blackert, R. Xu, B. I. Yakobson, and H. Zhu, Large effective magnetic fields from chiral phonons in rare-earth halides, arXiv:2306.03852.

[31] L. Allen, M. W. Beijersbergen, R. J. C. Spreeuw, and J. P. Woerdman, Orbital angular momentum of light and the transformation of Laguerre-Gaussian laser modes, Phys. Rev. A **45**, 8185 (1992).

[32] S. Franke-Arnold, 30 years of orbital angular momentum of light, Nat. Rev. Phys. **4**, 361 (2022).

[33] G. F. Quinteiro Rosen, P. I. Tamborenea, and T. Kuhn, Interplay between optical vortices and condensed matter, Rev. Mod. Phys. **94**, 035003 (2022).

[34] L. Paterson, M. P. MacDonald, J. Arlt, W. Sibbett, P. Bryant, and K. Dholakia, Controlled rotation of optically trapped microscopic particles, Science **292**, 912 (2001).

[35] M. P. MacDonald, L. Paterson, K. Volke-Sepulveda, J. Arlt, W. Sibbett, and K. Dholakia, Creation and manipulation of three-dimensional optically trapped structures, Science **296**, 1101 (2002).

[36] D. G. Grier, A revolution in optical manipulation, Nature (London) **424**, 810 (2003).

[37] W. Zhong, D. Vanderbilt, and K. M. Rabe, Phase transitions in $BaTiO_3$ from first principles, Phys. Rev. Lett. **73**, 1861 (1994).

[38] W. Zhong, D. Vanderbilt, and K. M. Rabe, First-principles theory of ferroelectric phase transitions for perovskites: The case of $BaTiO_3$, Phys. Rev. B **52**, 6301 (1995).

[39] A. Garcia and D. Vanderbilt, Electromechanical behavior of $BaTiO_3$ from first principles, Appl. Phys. Lett. **72**, 2981 (1998).

[40] L. Bellaiche, A. García, and D. Vanderbilt, Electric-field induced polarization paths in $Pb(Zr_{1-x}Ti_x)O_3$ alloys, Phys. Rev. B **64**, 060103(R) (2001).

[41] I. Kornev, H. Fu, and L. Bellaiche, Ultrathin films of ferroelectric solid solutions under a residual depolarizing field, Phys. Rev. Lett. **93**, 196104 (2004).

[42] I. I. Naumov, L. Bellaiche, and H. Fu, Unusual phase transitions in ferroelectric nanodisks and nanorods, Nature (London) **432**, 737 (2004).

[43] B.-K. Lai, I. Ponomareva, I. Naumov, I. Kornev, H. Fu, L. Bellaiche, and G. J. Salamo, Electric-field-induced domain evolution in ferroelectric ultrathin films, Phys. Rev. Lett. **96**, 137602 (2006).

[44] Y. Nahas, S. Prokhorenko, L. Louis, Z. Gui, I. Kornev, and L. Bellaiche, Discovery of stable skyrmionic state in ferroelectric nanocomposites, Nat. Commun. **6**, 8542 (2015).

[45] A. Gruverman, D. Wu, H. Fan, I. Vrejoiu, M. Alexe, R. Harrison, and J. Scott, Vortex ferroelectric domains, J. Phys. Condens. Matter **20**, 342201 (2008).

[46] B. Rodriguez, X. Gao, L. Liu, W. Lee, I. Naumov, A. Bratkovsky, D. Hesse, and M. Alexe, Vortex polarization states in nanoscale ferroelectric arrays, Nano Lett. **9**, 1127 (2009).

[47] Y. Ivry, D. P. Chu, J. F. Scott, and C. Durkan, Flux closure vortexlike domain structures in ferroelectric thin films, Phys. Rev. Lett. **104**, 207602 (2010).

[48] Q. Zhang, L. Xie, G. Liu, S. Prokhorenko, Y. Nahas, X. Pan, L. Bellaiche, A. Gruverman, and N. Valanoor, Nanoscale bubble domains and topological transitions in ultrathin ferroelectric films, Adv. Mater. **29**, 1702375 (2017).

[49] Y. Nahas, S. Prokhorenko, J. Fischer, B. Xu, C. Carrétéro, S. Prosandeev, M. Bibes, S. Fusil, B. Dkhil, V. Garcia *et al.*, Inverse transition of labyrinthine domain patterns in ferroelectric thin films, Nature (London) **577**, 47 (2020).

[50] W. Koshibae and N. Nagaosa, Creation of skyrmions and antiskyrmions by local heating, Nat. Commun. **5**, 5148 (2014).

[51] H. Fujita and M. Sato, Ultrafast generation of skyrmionic defects with vortex beams: Printing laser profiles on magnets, Phys. Rev. B **95**, 054421 (2017).

[52] See Supplemental Material at http://link.aps.org/supplemental/10.1103/PhysRevLett.131.196801 for computational details, derivation of dynamical multiferroicity, orbital magnetic moments and their topological characterization, and the robustness of the mechanism.

[53] B. Xu, J. Íñiguez, and L. Bellaiche, Designing lead-free antiferroelectrics for energy storage, Nat. Commun. **8**, 15682 (2017).

[54] Z. Jiang, Y. Nahas, S. Prokhorenko, S. Prosandeev, D. Wang, J. Íñiguez, and L. Bellaiche, Giant electrocaloric response in the prototypical $Pb(Mg,Nb)O_3$ relaxor ferroelectric from atomistic simulations, Phys. Rev. B **97**, 104110 (2018).

[55] V. Garcia, S. Fusil, K. Bouzehouane, S. Enouz-Vedrenne, N. D. Mathur, A. Barthelemy, and M. Bibes, Giant tunnel electroresistance for non-destructive readout of ferroelectric states, Nature (London) **460**, 81 (2009).

[56] A. Chanthbouala, A. Crassous, V. Garcia, K. Bouzehouane, S. Fusil, X. Moya, J. Allibe, B. Dlubak, J. Grollier, S. Xavier *et al.*, Solid-state memories based on ferroelectric tunnel junctions, Nat. Nanotechnol. **7**, 101 (2012).

[57] V. Garcia and M. Bibes, Ferroelectric tunnel junctions for information storage and processing, Nat. Commun. **5**, 4289 (2014).

[58] D. Edwards, N. Browne, K. M. Holsgrove, A. B. Naden, S. O. Sayedghaee, B. Xu, S. Prosandeev, D. Wang, D. Mazumdar, M. Duchamp *et al.*, Giant resistive switching in mixed phase $BiFeO_3$ via phase population control, Nanoscale **10**, 17629 (2018).

[59] R. Mankowsky, A. von Hoegen, M. Först, and A. Cavalleri, Ultrafast reversal of the ferroelectric polarization, Phys. Rev. Lett. **118**, 197601 (2017).

[60] P. Chen, C. Paillard, H. J. Zhao, J. Íñiguez, and L. Bellaiche, Deterministic control of ferroelectric polarization by ultrafast laser pulses, Nat. Commun. **13**, 2566 (2022).

[61] S. Prosandeev, J. Grollier, D. Talbayev, B. Dkhil, and L. Bellaiche, Ultrafast neuromorphic dynamics using hidden phases in the prototype of relaxor ferroelectrics, Phys. Rev. Lett. **126**, 027602 (2021).

[62] F. Mayer, M. Deluca, and M. N. Popov, Hidden phases in homovalent and heterovalent substituted $BaTiO_3$, Phys. Rev. B **107**, 184307 (2023).

[63] A. Rusina, M. Durach, K. A. Nelson, and M. I. Stockman, Nanoconcentration of terahertz radiation in plasmonic waveguides, Opt. Express **16**, 18576 (2008).

[64] M. Schnell, P. Alonso-Gonzalez, L. Arzubiaga, F. Casanova, L. E. Hueso, A. Chuvilin, and R. Hillenbrand, Nanofocusing of mid-infrared energy with tapered transmission lines, Nat. Photonics **5**, 283 (2011).

[65] A. Toma, S. Tuccio, M. Prato, F. De Donato, A. Perucchi, P. Di Pietro, S. Marras, C. Liberale, R. Proietti Zaccaria, F. De Angelis *et al.*, Squeezing terahertz light into nanovolumes: Nanoantenna enhanced terahertz spectroscopy (nets) of semiconductor quantum dots, Nano Lett. **15**, 386 (2015).

[66] D. K. Gramotnev and S. I. Bozhevolnyi, Plasmonics beyond the diffraction limit, Nat. Photonics **4**, 83 (2010).

[67] L. Novotny and N. Van Hulst, Antennas for light, Nat. Photonics **5**, 83 (2011).

[68] R. W. Heeres and V. Zwiller, Subwavelength focusing of light with orbital angular momentum, Nano Lett. **14**, 4598 (2014).

[69] M. Pu, X. Ma, Z. Zhao, X. Li, Y. Wang, H. Gao, C. Hu, P. Gao, C. Wang, and X. Luo, Near-field collimation of light carrying orbital angular momentum with bull's-eye-assisted plasmonic coaxial waveguides, Sci. Rep. **5**, 1 (2015).

[70] D. Garoli, P. Zilio, Y. Gorodetski, F. Tantussi, and F. De Angelis, Optical vortex beam generator at nanoscale level, Sci. Rep. **6**, 1 (2016).

[71] G. Spektor, D. Kilbane, A. Mahro, B. Frank, S. Ristok, L. Gal, P. Kahl, D. Podbiel, S. Mathias, H. Giessen *et al.*, Revealing the subfemtosecond dynamics of orbital angular momentum in nanoplasmonic vortices, Science **355**, 1187 (2017).

[72] J. A. Hachtel, S.-Y. Cho, R. B. Davidson, M. A. Feldman, M. F. Chisholm, R. F. Haglund, J. C. Idrobo, S. T. Pantelides, and B. J. Lawrie, Spatially and spectrally resolved orbital angular momentum interactions in plasmonic vortex generators, Light. Light. **8**, 33 (2019).

[73] Y. Mukai, H. Hirori, T. Yamamoto, H. Kageyama, and K. Tanaka, Nonlinear magnetization dynamics of antiferromagnetic spin resonance induced by intense terahertz magnetic field, New J. Phys. **18**, 013045 (2016).

[74] S. Lang, W. Zhu, and Z.-G. Ye, Specific heat of ferroelectric $Pb(Zr_{1-x}Ti_x)O_3$ ceramics across the morphotropic phase boundary, J. Appl. Phys. **111**, 094102 (2012).

[75] H. Fujita and M. Sato, Encoding orbital angular momentum of light in magnets, Phys. Rev. B **96**, 060407(R) (2017).

[76] D. J. Griffiths, *Introduction to Electrodynamics* (Prentice-Hall, Englewood Cliffs, 1999), Chap. 5, p. 228.

[77] D. J. Griffiths, *Introduction to Electrodynamics* (Prentice-Hall, Englewood Cliffs, 1999), Chap. 10, p. 340.

[78] L. F. Richardson, IX. The approximate arithmetical solution by finite differences of physical problems involving differential equations, with an application to the stresses in a masonry dam, Phil. Trans. R. Soc. A **210**, 307 (1911).

[79] L. F. Richardson and J. A. Gaunt, VIII. The deferred approach to the limit, Phil. Trans. R. Soc. A **226**, 299 (1927).

[80] D. M. Juraschek, Q. N. Meier, M. Trassin, S. E. Trolier-McKinstry, C. L. Degen, and N. A. Spaldin, Dynamical magnetic field accompanying the motion of ferroelectric domain walls, Phys. Rev. Lett. **123**, 127601 (2019).

[81] B. Berg and M. Lüscher, Definition and statistical distributions of a topological number in the lattice O(3) σ-model, Nucl. Phys. **B190**, 412 (1981).

[82] D. L. Andrews, *Structured Light and Its Applications: An Introduction to Phase-Structured Beams and Nanoscale Optical Forces* (Academic Press, New York, 2011).

[83] K. Shintani, K. Taguchi, Y. Tanaka, and Y. Kawaguchi, Spin and charge transport induced by a twisted light beam on the surface of a topological insulator, Phys. Rev. B **93**, 195415 (2016).

[84] D. J. Griffiths, *Introduction to Electrodynamics* (Prentice-Hall, Englewood Cliffs, 1999).

[85] L. Gao, S. Prokhorenko, Y. Nahas, and L. Bellaiche, Dynamical control of topology in ferroelectric skyrmions via twisted light, arXiv:2302.01402.

[86] K. Moon, H. Mori, K. Yang, S. M. Girvin, A. H. MacDonald, L. Zheng, D. Yoshioka, and S.-C. Zhang, Spontaneous interlayer coherence in double-layer quantum hall systems: Charged vortices and kosterlitz-thouless phase transitions, Phys. Rev. B **51**, 5138 (1995).

[87] T. Senthil, A. Vishwanath, L. Balents, S. Sachdev, and M. P. Fisher, Deconfined quantum critical points, Science **303**, 1490 (2004).

[88] O. A. Tretiakov and O. Tchernyshyov, Vortices in thin ferromagnetic films and the skyrmion number, Phys. Rev. B **75**, 012408 (2007).

[89] C. Phatak, A. K. Petford-Long, and O. Heinonen, Direct observation of unconventional topological spin structure in coupled magnetic discs, Phys. Rev. Lett. **108**, 067205 (2012).

[90] F. Hellman, A. Hoffmann, Y. Tserkovnyak, G. S. Beach, E. E. Fullerton, C. Leighton, A. H. MacDonald, D. C. Ralph, D. A. Arena, H. A. Dürr *et al.*, Interface-induced phenomena in magnetism, Rev. Mod. Phys. **89**, 025006 (2017).

[91] F. P. Chmiel, N. Waterfield Price, R. D. Johnson, A. D. Lamirand, J. Schad, G. van der Laan, D. T. Harris, J. Irwin, M. S. Rzchowski, C.-B. Eom *et al.*, Observation of magnetic vortex pairs at room temperature in a planar α-Fe_2O_3/Co heterostructure, Nat. Mater. **17**, 581 (2018).

[92] X. Yu, W. Koshibae, Y. Tokunaga, K. Shibata, Y. Taguchi, N. Nagaosa, and Y. Tokura, Transformation between meron and skyrmion topological spin textures in a chiral magnet, Nature (London) **564**, 95 (2018).

[93] X. Lu, R. Fei, L. Zhu, and L. Yang, Meron-like topological spin defects in monolayer $CrCl_3$, Nat. Commun. **11**, 4724 (2020).

[94] T. Eggebrecht, M. Möller, J. G. Gatzmann, N. R. da Silva, A. Feist, U. Martens, H. Ulrichs, M. Münzenberg, C. Ropers, and S. Schäfer, Light-induced metastable magnetic texture uncovered by *in situ* lorentz microscopy, Phys. Rev. Lett. **118**, 097203 (2017).

[95] G. Berruto, I. Madan, Y. Murooka, G. Vanacore, E. Pomarico, J. Rajeswari, R. Lamb, P. Huang, A. Kruchkov, Y. Togawa *et al.*, Laser-induced skyrmion writing and erasing in an ultrafast cryo-Lorentz transmission electron microscope, Phys. Rev. Lett. **120**, 117201 (2018).

[96] J. Tang, L. Kong, W. Wang, H. Du, and M. Tian, Lorentz transmission electron microscopy for magnetic skyrmions imaging, Chin. Phys. B **28**, 087503 (2019).

[97] T. R. Harvey, N. Rubiano da Silva, J. H. Gaida, M. Möller, A. Feist, S. Schäfer, and C. Ropers, Ultrafast electron microscopy for probing magnetic dynamics, MRS Bull. **46**, 711 (2021).